An experimentally validated electro-thermal EV battery pack model incorporating cycle-life aging and cell-to-cell variations

Joseph N. E. Lucero[1,4], *Student Member, IEEE*, Vivek A. Sujan[2], *Senior Member, IEEE*, and Simona Onori[3,4,*], *Senior Member, IEEE*

***Abstract*—Lithium-ion batteries are used in a wide variety of applications. To meet the power and energy demands of these applications battery packs are composed of hundreds to thousands of cells. The electrical and thermal interactions between cells introduce additional complexity in the pack dynamics. To capture these effects, a battery pack model composed of 192 cells based on a first-generation (2012) Nissan Leaf battery pack is developed in MATLAB/Simulink/Simscape. With this model, we simulate the electrical dynamics (using a first-order equivalent-circuit model), the thermal dynamics (using a first-order lumped-parameter thermal model), and the aging dynamics (using a semi-empirical severity factor-based model) of every cell in the pack and we also create a pack thermal model that explicitly captures the heat exchange between the modules, and the cells contained within, during operation. The models are calibrated and validated, both at the cell and pack level, with experimental data. Two different case studies of this pack model are investigated. In the first case study, an initial, normally-distributed, cell-to-cell capacity variation is introduced and its effect on the pack voltage and module temperatures is studied. In the second case study, we deliberately insert cells with lower than nominal capacity into the pack and we investigate how this type of initial cell-to-cell capacity variation affects the pack's ability to deliver energy over time. Finally, we also study how parallel-connected cells can reduce the effects of cell-to-cell variations at the expense of increased aging of the pack overall.**

NOMENCLATURE

i	Integer index of the cells in the pack
$\mathrm{SoC}^{(i)}$	State-of-charge of the ith cell [%]
$Q^{(i)}$	Capacity of the ith cell [Ah]
$I_{\mathrm{cell}}^{(i)}$	Current through the ith cell ($I_{\mathrm{cell}}^{(i)} > 0$: discharge, $I_{\mathrm{cell}}^{(i)} < 0$: charge) [A]
I_{pack}	Current through the pack [A]
$V_{\mathrm{RC}}^{(i)}$	Diffusion voltage of the ith cell [V]
$\tau_1^{(i)}$	Voltage relaxation time of the ith cell [s]
$C_1^{(i)}$	Capacitance of the ith cell [F]
$V_{\mathrm{cell}}^{(i)}$	Terminal voltage of the ith cell [V]
V_{pack}	Terminal voltage of the pack [V]
$R_0^{(i)}$	High-frequency resistance (HFR) of the ith cell [Ω]
$\mathrm{Wh}_{\mathrm{dchg}}^{(i)}$	Discharge energy-throughput of the ith cell [Wh]
$Q_{\mathrm{loss}}^{(i)}$	Normalized capacity fade of the ith cell [%]
$R_{\mathrm{incr}}^{(i)}$	Normalized high-frequency resistance increase of the ith cell [%]
f_{s}	Sampling frequency at which measurements are collected [Hz]
T_{tot}	Total time that measurements are collected [s]
N_{meas}	Total number of measurements collected
T_{amb}	Ambient air temperature [°C]
T_{pack}	Temperature of the pack enclosure [°C]
T_{module}	Temperature of the module enclosure [°C]
T_{cell}	Surface temperature of a single cell [°C]
C_{pack}	Effective heat capacity of the pack enclosure [J/°C]
C_{module}	Effective heat capacity of module enclosure [J/°C]
C_{cell}	Effective heat capacity of a single cell [J/°C]
R_{cc}	Thermal resistance of heat exchange between cells [°C/W]
R_{mc}	Thermal resistance of heat exchange between cell and the module housing [°C/W]
R_{mm}	Thermal resistance of heat exchange between modules [°C/W]
R_{pm}	Thermal resistance of heat exchange between module and the pack enclosure [°C/W]
R_{d}	Thermal resistance of heat exchange between pack enclosure and the ambient air [°C/W]
$E(t)$	Energy delivered by a battery pack [Wh]
RMSE	Root mean-square error between model output and the experimental data
RMSPE	Root mean-square percent error between model output and the experimental data
$\mathcal{N}(x;\mu,\Sigma_x)$	Normal distribution of a scalar random variable x with mean μ and scalar variance Σ_x.

[1] Chemistry, Stanford University, Stanford, CA.
[2] National Transportation Research Center, Oak Ridge National Lab, Oak Ridge, TN.
[3] Energy Science & Engineering, Stanford University, Stanford, CA.
[4]Applied Energy Division, Energy Science Directorate – SLAC National Accelerator Laboratory
[*] corresponding author sonori@stanford.edu

I. INTRODUCTION

Prompted by increasing concerns over pollution and greenhouse gas emissions, automotive companies are transitioning away from traditional internal-combustion engine vehicles and towards electrified powertrains [1]. The lithium-ion battery has come to be the predominant energy storage technology used electric vehicles (EVs), due to its superior energy and power densities, as well as longevity, compared to other battery types [2].

In the transportation sector, heavy-duty commercial vehicles (HDCVs) have been identified by previous studies to be a prime candidate for electrification [3], [4]. Specifically, battery electric trucks have been projected to be suitable for drayage applications where these trucks would operate within a roughly 250 mile radius of an intermodal hub such as a seaport. One report [5] focusing around the port of New York and New Jersey estimates that, if commercial vehicle fleets operating around the port were to have 100% electrification adoption, there would be a 75% reduction in carbon-dioxide emissions relative to that of the currently in-use fossil-fuel based fleets. Work is currently underway to better understand the energy and infrastructure requirements for effective electrification of HDCV fleets [6], [7].

Battery *cells* must be connected electrically in a battery *module*, and modules are subsequently connected to form a battery *pack*[1]. Voltage, current and temperature sensors are placed at various levels of this hierarchy to enable monitoring of the battery states [9]. Due to volume constraints, cells/modules are arranged to be in close spatial proximity to one another leading them to exchange heat [10]. To maximize efficiency, longevity, and reliability of the battery pack, minimization of cell-to-cell variation is important [11]–[13]. In this article, we use "cell-to-cell variation" to refer to the differences in properties of battery cells, often arising from differences in process manufacturing [14]. This translates into a difference in parameters of the dynamic model used to represent the battery. In particular, cell-to-cell variations within a module have been shown to lead to a lack of thermal uniformity contributing to heterogeneous aging of cells [15]. Severe cell-to-cell variation can thus affect the durability and long-term performance of battery packs.

To model and predict the electrical dynamics of battery cells, equivalent-circuit models (ECM) are generally used [16]. ECMs provide a simple framework that captures the voltage dynamics of a battery when calibrated to experimentally-collected data [17]. Importantly, as this approach is entirely empirical, it cannot be used to reliably predict the electrical dynamics in operating regimes which are not covered by the data used to calibrate the model. Alternatively, physics-based models (PBMs) can be used to model the electrochemical dynamics more reliably across a wide-range of operating conditions while using less experimental data; however, this type of model has a more complex mathematical structure and generally requires higher computational effort [16]. ECMs can be augmented with models that capture the thermal and aging dynamics of the battery cell. To model the temperature changes of the battery cell during operation, lumped-parameter thermal models are often used [18]. To capture the aging (capacity and power fade) of battery cells, it is common to use either semi-empirical [19]–[22] or machine-learning based approaches [23], [24].

To construct a battery pack model for use in system-level applications, battery cell models are often upscaled to the pack by assuming the ideal scenario: All the cells in the pack are created equal and that the temperature of each cell is unaffected by the temperatures of other cells. This assumption neglects any cell-to-cell variations and the details of the inter-dependence of the cells' temperature dynamics, but ultimately gives simple relations that directly relate the pack current, voltage, and temperature to that of the cell [25]:

$$I_{\text{pack}} = N_{\text{parallel}} \cdot I_{\text{cell}} \tag{1a}$$

$$V_{\text{pack}} = N_{\text{series}} \cdot V_{\text{cell}} \tag{1b}$$

$$T_{\text{pack}} = T_{\text{cell}} \ , \tag{1c}$$

where the variables N_{series} and N_{parallel} are the number of cells that are connected in series and parallel, respectively. We refer to the battery pack model described by (1) as the "ideal" pack model. This approach has been used in many previous vehicle/system level studies [26]–[28]; however, the degree of fidelity-loss at the vehicle level when using battery pack models developed using this assumption is currently unclear. The development and calibration of realistic battery pack models is hindered by lack of publicly available data. Nevertheless, previous studies have sought to explore the effects of cell-to-cell variations in various ways. For example, the authors of [29] construct a 3S3P battery module where the electrical, thermal, and aging dynamics are modeled for each cell in the module. In this study, they find that varying the initial capacity of the cells in the module by 5% results in an 8% SoC imbalance and a 3°C variance in temperature across the battery cells of the module after a discharge cycle. Another study [30] uses an electro-thermal-aging pack model to study how typical highway and city driving conditions affects battery thermal management system usage. To validate the pack's thermal model, the authors use a scaled-down protocol using only a single module from the battery pack and do not provide validation for the electrical or aging models. The authors of [31] study the effects of initial cell-to-cell capacity and impedance variations on the energy utilization of a battery pack showing that parallel-connected cells reduce the initial relative cell parameter variance, reaching the same conclusion as [32]. Their pack model however, does not model the thermal retroactivity [15], [33].

A clear gap in the literature remains: while battery pack models have previously been constructed using data from individual cells, they have not been validated with experimental data from a full battery pack experiencing realistic drive-cycle loads. Summarily, the contributions of this paper are the following:

1) A model (in MATLAB/Simulink/Simscape) that captures the integrated electrical, thermal, and aging dynamics of individual Lithium Manganese Oxide (LMO) cells used in the Nissan Leaf battery pack is created. The integrated model of the cell is validated with experimental data over a range of ambient temperature and aging conditions.
2) Implementation and calibration of a simulator for a first-generation Nissan Leaf battery pack (Fig. 1) constructed from individual cell models. A detailed lumped-parameter thermal model is created to capture the heat exchange between the cells and modules within the pack. The pack's voltage and temperature dynamics are validated

[1]Cell-to-pack battery configurations where individual cells are directly assembled into a pack, without modular subdivisions, also exist [8]

with experimental data.

3) An investigation into the effects of introducing cell-to-cell capacity variation into the cells of a fresh pack on the dynamical response of the cells and the pack overall.

The remainder of the article is organized as follows: Section II details the organization of cells and modules within the Nissan Leaf battery pack. Subsequently, it discusses the relevant details of the experiments done for cells and pack at Idaho National Lab (INL) [10]. In Section III, the battery cell model which integrates the electrical (III-A), thermal (III-B), and aging (III-C) dynamics is described. In Section IV, how the battery cells and modules within the pack are electrically connected is introduced and a detailed model capturing the heat exchange between the cells and modules is established. The pack model voltage and temperature outputs are then validated in Section IV-B. We then explore two case studies using this pack model. Firstly, in Section V, the effects of cell-to-cell capacity variation on both the fresh pack's dynamics (Section V-A), as well as how it affects cell-level (Section V-B) properties are investigated. Secondly, in Section VI, we explore the effect of deliberately adding cells with known decreased capacity (Section VI-A) and comparing the energy utilization of this pack with an ideal pack model (1) assuming that all other common parameters of the two models are equal. We then investigate how parallel-connected cells leads to the observed pack energy utilization trends (Section VI-B).

II. Battery Pack Configuration

In this section, we detail the cell specifications, the module configuration within the battery pack followed by the description of cell and pack experimental data collected at INL.

A. Pack configuration

The battery pack of the (2012) first-generation Nissan Leaf consists of 192 battery cells with a graphite negative electrode and a LMO positive electrode [10]. Four cells are pressed together, one on top of another, electrically connected into a 2P2S electrical configuration, and enclosed in an aluminum casing to form a battery module. 48 of these battery modules are then connected electrically in series to form the full pack. Cell and pack specifications are summarized in Table I [10]. Figure 1 illustrates how the modules are spatially organized within the pack enclosure. Towards the rear of the pack, there is a module stack (Stack 1) consisting of 24 battery modules that are oriented vertically. The remaining 24 modules, are organized into four distinct stacks. Two of the stacks (2 & 5) consists of two columns where each column consists of two horizontally-oriented modules. Similarly, the remaining 2 stacks located at the very front of the pack (3 & 4), consists of two columns where each column consists of four horizontally-oriented modules [34]. The positive terminal of the pack originates in Stack 1 while the pack negative terminal originates in Stack 5 (Fig. 1b, encircled + and −). The terminal voltage is measured as the difference in voltage between the positive and negative terminals[2].

[2]Note that the spatial arrangement of these modules need not be directly related to how these modules are electrically connected.

TABLE I: Specifications of battery pack and cells [10].

Battery pack specs	
Manufacturer	Nissan
Positive electrode	$LiMn_2O_4$
Negative electrode	LiC_6
Module electrical configuration	2P2S
Pack electrical configuration	48S1P
Total number of cells in pack	192
Nominal capacity (Ah) cell/pack	33.1/66.2
Nominal voltage (V) cell/pack	3.8/364.8
Charge cutoff voltage (V) cell/pack	4.11/395
Discharge cutoff voltage (V) cell/pack	2.5/285
Pack cooling mechanism	Free convection

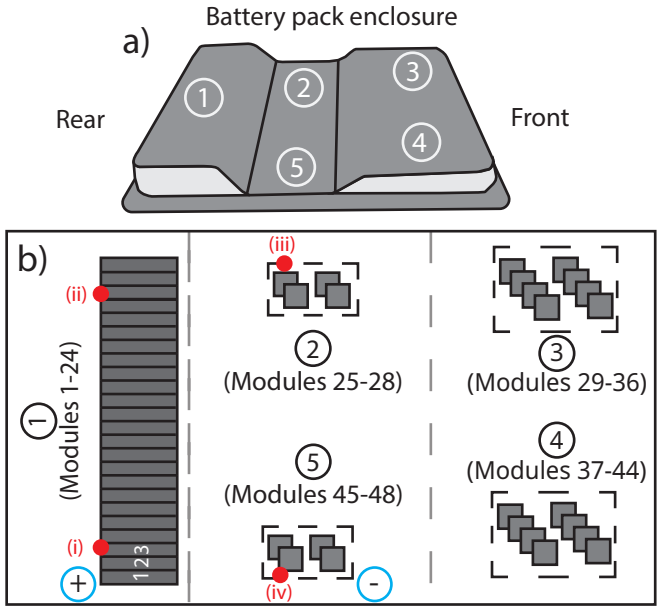

*Fig. 1: **Pack configuration.** a) Nissan Leaf battery pack with locations of module stacks numbered. b) Detailed organization of the module stacks in the battery pack. In Stack 1 all modules are stacked vertically. Partially occluded squares in Stacks 2-5 indicate horizontally stacked modules. The positive terminal of the pack, denoted by the circled +, is located at module 1 (numbered) in Stack 1. The negative terminal, denoted by the circled −, is located at module 48 in Stack 5. The positive and negative terminal wires are routed to the front of the pack where the pack is connected to the drivetrain. The red dots with corresponding roman numerals (i.e., (I), (II), (III), (IV)) denote the placement of the four thermocouples used to measure module/pack temperatures during the experiment.*

We note that the described organization of these modules implies that some modules have two nearest-neighbors while others (eg. the modules at the top and bottom of a module tower) will only have one nearest neighbor. This implies a difference in the thermal interactions of these modules relative to ones that have two nearest neighbors. The battery pack thermal model that we develop in Section IV accounts for this distinction.

B. Cell and pack data

An aging campaign [10] was carried out over a one-year period, where the battery pack was subjected to drive-cycle

based aging. Specifically, a power-based cycle (corresponding current input shown in Fig. 4a) which simulates an on-road Nissan Leaf drive cycle was used [35]. During the drive cycle, the pack experiences a maximum C-rate, defined as the maximum current applied to the pack normalized by the pack's nominal capacity, of 3.5C and an average C-rate of 0.2C[3]. After discharge, the pack is charged with a constant-current step of 120A, and a subsequent voltage hold at 395 V until the current tapered off to less than 0.3A or lower for up to an hour, which is then followed by a long rest period. Characterization data was collected both at the pack and at the cell level (using isolated cells) at a roughly monthly interval. Specifically, for the cells, three fixed ambient temperatures, 20, 30, and 40°C are used for the aging and characterization experiments with three replicates per temperature. For the pack, the aging and characterization occurs at a fixed ambient temperature of 30°C. The experiments show that cells in the pack experience a higher range of temperatures compared to that of isolated cells experiencing the same (scaled) input load. This higher temperature leads to accelerated aging of the cell in the pack relative to that of isolated cells.

III. Battery Cell Model

In this section, we outline the electrical, thermal and aging submodels for the battery cell, which interact according to Fig. 2.

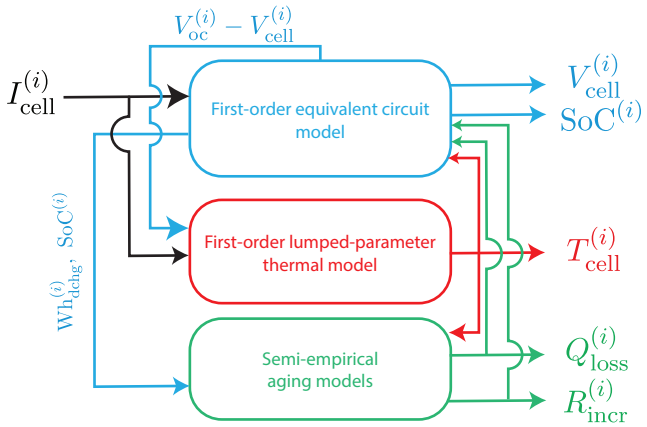

Fig. 2: Schematic showing the interdependencies of the electrical, thermal, and aging submodels for a single battery cell.

A. Electrical submodel

The cell-level electrical dynamics are modeled using a first-order ECM, whose equations for the ith cell are [36],

$$\frac{\mathrm{d}}{\mathrm{d}t}V_{\mathrm{RC}}^{(i)}(t) = -\frac{1}{\tau_1(\mathrm{SoC}^{(i)})}V_{\mathrm{RC}}^{(i)}(t) + \frac{1}{C_1(\mathrm{SoC}^{(i)})}I_{\mathrm{cell}}^{(i)}(t) \tag{2a}$$

$$V_{\mathrm{cell}}^{(i)}(t) = V_{\mathrm{oc}}(\mathrm{SoC}^{(i)}) - V_{\mathrm{RC}}^{(i)}(t) - I_{\mathrm{cell}}^{(i)}(t)R_0(\mathrm{SoC}^{(i)}, T_{\mathrm{cell}}^{(i)}) \ . \tag{2b}$$

[3]Assuming an ideal pack, the pack C-rate is equivalent to the cell C-rate.

Equation (2a) models the dynamics of the diffusion voltage $V_{\mathrm{RC}}^{(i)}(t)$ given a timescale $\tau_1 = R_1C_1$ and an input current $I_{\mathrm{cell}}^{(i)}(t)$. The resistance of the RC loop is denoted by R_1 and the capacitance is denoted as C_1. Both these quantities depend on the state-of-charge $\mathrm{SoC}^{(i)}$ of the battery cell, which is tracked by Coulomb counting

$$\frac{\mathrm{d}}{\mathrm{d}t}\mathrm{SoC}^{(i)}(t) = -\frac{1}{3600 \cdot Q^{(i)}}I_{\mathrm{cell}}^{(i)}(t) \ . \tag{3}$$

The capacity of the cell (measured in units of Ampere-hour) is denoted by $Q^{(i)}$ in (3). The terminal voltage (2b) depends on the diffusion voltage $V_{\mathrm{RC}}(t)$, the relationship between the open-circuit voltage and SoC, $V_{\mathrm{oc}}(\mathrm{SoC}^{(i)})$, which in this work is calculated from $C/3$ discharge capacity test data (Fig. 11), as well as the high-frequency resistance (HFR), $R_0(\mathrm{SoC}^{(i)}, T_{\mathrm{cell}}^{(i)})$. The HFR is calculated for every pusle (i.e., at different SoC levels)in the HPPC test as,

$$R_0(\mathrm{SoC}^{(i)}, T_{\mathrm{cell}}^{(i)}) = \frac{V_{\mathrm{cell}}^{(i)}(t+\Delta t) - V_{\mathrm{cell}}^{(i)}(t)}{I_{\mathrm{cell}}^{(i)}(t+\Delta t) - I_{\mathrm{cell}}^{(i)}(t)}, \tag{4}$$

where the sampling time of the measurements is $\Delta t = 0.1$ s and the cell surface temperature $T_{\mathrm{cell}}^{(i)}$. The dynamics of $T_{\mathrm{cell}}^{(i)}$ are described in Section III-B. Throughout this article, we use the convention that positive (negative) current $I_{\mathrm{cell}}^{(i)} > 0$ ($I_{\mathrm{cell}}^{(i)} < 0$) corresponds to battery discharge (charge). As there are 192 total cells in the pack, $i \in \{1, 2, \ldots, 192\}$. The parameters R_0, τ_1 and C_1 of the electrical submodel are calibrated to experimental data as discussed in Appendix A[4].

B. Thermal submodel

To model the cell's surface temperature dynamics we assume a one-state lumped parameter thermal model [37], [38]:

$$C_{\mathrm{cell}}\frac{\mathrm{d}}{\mathrm{d}t}T_{\mathrm{cell}}^{(i)}(t) = I_{\mathrm{cell}}^{(i)}(t)\left[V_{\mathrm{oc}}^{(i)}(\mathrm{SoC}^{(i)}) - V_{\mathrm{cell}}^{(i)}(t)\right] + \frac{1}{R_{\mathrm{mc}}}\left[T_{\mathrm{amb}} - T_{\mathrm{cell}}^{(i)}(t)\right] \ . \tag{5}$$

Here, C_{cell} denotes the cell's heat capacity, R_{mc} denotes the convective resistance between the cell and its surroundings, and T_{amb} denotes the ambient temperature. The first term on the right-hand side (RHS) of (5) models the Joule heating of the battery during operation while the second term models the heat exchange between the cell and its surroundings. Both parameters C_{cell} and R_{mc} of the cell model are calibrated to experimental data as described in Appendix A.

C. Aging submodel

The degradation of a battery cell through usage is characterized by a decreasing capacity, often called capacity fade, and a decreasing power output arising from an increase in HFR [39].

[4]The parameters of the ECM model R_0, τ_1 and C_1, as well as the open circuit voltage V_{oc} are all functions of the cell's SoC. We assume that the relationship between these variables and SoC is the same for all cells; however, when cells are connected in a pack (Section IV) we allow for the possibility that different cells in the pack can have different SoCs, and thus experience a different value of these parameters, at a particular point in time.

The degree of usage of the battery cell is quantified here by the discharge energy throughput (only for $I_{\text{cell}}^{(i)} > 0$)[5],

$$\text{Wh}_{\text{dchg}}^{(i)}(t) = \frac{1}{3600}\int_0^t I_{\text{cell}}^{(i)}(s)V_{\text{cell}}^{(i)}(s)\,\text{d}s \ . \tag{6}$$

The cell's beginning of life (BOL) is defined to be $\text{Wh}_{\text{dchg}}^{(i)} = 0$.

The capacity fade of the ith cell is defined as the capacity of the ith cell normalized to its value at BOL,

$$Q_{\text{loss}} = 100\frac{Q^{(i)}(\text{Wh}_{\text{dchg}}^{(i)} = 0, T_{\text{cell}}^{(i)}) - Q^{(i)}(\text{Wh}_{\text{dchg}}^{(i)}, T_{\text{cell}}^{(i)})}{Q^{(i)}(\text{Wh}_{\text{dchg}}^{(i)} = 0, T_{\text{cell}}^{(i)})} \ , \tag{7}$$

where $Q^{(i)}(\text{Wh}_{\text{dchg}}^{(i)}, T_{\text{cell}}^{(i)})$ is the capacity of the battery after being subjected to an amount of discharge energy throughput $\text{Wh}_{\text{dchg}}^{(i)}$ at a temperature $T_{\text{cell}}^{(i)}$ and $Q^{(i)}(\text{Wh}_{\text{dchg}}^{(i)} = 0, T_{\text{cell}}^{(i)})$ is the cell's BOL capacity. Similarly, the HFR increase of the ith cell is defined as the HFR of the ith cell normalized to its BOL value,

$$R_{0,\text{incr}}^{(i)} = 100\frac{R_0(\text{SoC}^{(i)}, T_{\text{cell}}^{(i)}, \text{Wh}_{\text{dchg}}^{(i)}) - R_0^{\text{init}}(\text{SoC}^{(i)}, T_{\text{cell}}^{(i)})}{R_0^{\text{init}}(\text{SoC}^{(i)}, T_{\text{cell}}^{(i)})} \ , \tag{8}$$

where $R_0(\text{SoC}^{(i)}, T_{\text{cell}}^{(i)}, \text{Wh}_{\text{dchg}}^{(i)})$ is the cell's HFR value after being subjected to an amount of discharge energy throughput $\text{Wh}_{\text{dchg}}^{(i)}$ at a temperature $T_{\text{cell}}^{(i)}$ at $\text{SoC}^{(i)}$. The cell's BOL HFR value is denoted as $R_0^{\text{init}}(\text{SoC}^{(i)}, T_{\text{cell}}^{(i)}) = R_0(\text{SoC}^{(i)}, T_{\text{cell}}^{(i)}, \text{Wh}_{\text{dchg}}^{(i)} = 0)$.

The capacity fade (7) is modeled as a power law in the discharge energy throughput with exponent ζ_Q [20],

$$Q_{\text{loss}}^{(i)} = \sigma_Q(T_{\text{cell}}^{(i)})\left[\text{Wh}_{\text{dchg}}^{(i)}\right]^{\zeta_Q} \ , \tag{9}$$

and with a cell surface temperature-dependent Arrhenius-like severity factor function,

$$\sigma_Q(T_{\text{cell}}^{(i)}) = \gamma_Q \exp\left(-\frac{\alpha_Q}{T_{\text{cell}}^{(i)}}\right) \ . \tag{10}$$

The scalar term in the exponential α_Q is equal to $E_{\text{A},Q}/R$, where $E_{\text{A,Q}}$ is the effective activation energy characterizing the capacity fade and R is the universal gas constant. Similarly, γ_Q is a scalar. Both scalars are calibrated to experimental data as shown in Appendix A. Intuitively, the discharge energy throughput quantifies the accumulated damage to the battery cell due to usage. The accumulated damage quantified by the discharge-energy throughput is scaled based on the conditions at which usage occurs and this is modeled through the severity factor [40]. We model the HFR increase (8) of the battery cells using a semi-empirical model in the form of a power law,

$$R_{0,\text{incr}}^{(i)} = \sigma_{R_0}(\text{SoC}^{(i)}, T_{\text{cell}}^{(i)})\left[\text{Wh}_{\text{dchg}}^{(i)}\right]^{\zeta_{R_0}} \ , \tag{11}$$

with exponent ζ_{R_0} and where the HFR increase severity factor function $\sigma_{R_0}(\text{SoC}^{(i)}, T_{\text{cell}}^{(i)})$ depends on both the cell $\text{SoC}^{(i)}$ and temperature $T_{\text{cell}}^{(i)}$ as follows:

$$\sigma_{R_0}(\text{SoC}^{(i)}, T_{\text{cell}}^{(i)}) = \left|\sum_{j=0}^{4}\theta_{1j}\cdot(\text{SoC}^{(i)})^j\right| \times \exp\left(\sum_{k=0}^{4}\theta_{2k}\cdot(\text{SoC}^{(i)})^k\right)\exp\left(-\frac{\alpha_{R_0}}{T_{\text{cell}}^{(i)}}\right) \ . \tag{12}$$

Here, $\theta_{1j},\ j \in [1,4]$ and $\theta_{2k},\ k \in [1,4]$ are scalars, and the scalar term α_{R_0} is equal to $E_{\text{A},R_0}/R$. These scalars are calibrated to experimental data in Appendix A. The absolute value on the outer polynomial ensures that the severity factor is always positive, encoding the assumption that usage should not decrease the degree of aging. We calibrate the electric, thermal, and aging sub-models for a single battery cell using experimental data, as discussed in Appendix A. The integrated electro-thermal-aging model for the battery cell is then validated across a wide range of temperatures and aging conditions in Appendix B.

IV. Battery Pack Model and Validation

From the individual battery cell model, in this section, the battery pack model is assembled to the specifications of the Nissan Leaf battery pack. Specifically, the electrical connections and thermal models that describe the heat exchange between the cells and modules in the pack are first described (Section IV-A) and the resulting pack model is subsequently validated (Section IV-B). Importantly, capturing the heat exchange between the cells allows for greater fidelity in tracking the propagation of cell-to-cell variations as the battery pack is used. For details of the battery pack thermal model calibration, the reader is referred to Appendix C.

A. Battery Pack Model Configuration

Electrically, the pack model is formed by first connecting 192 cells in a 2P2S configuration to form 48 modules. The 48 modules are then connected in series (Fig. 1). The electrical connections and thermal interactions between the components of the pack are modeled using custom-made Simscape elements[6]. The heat exchange between the pack, the modules, and the cells are described in the remainder of this section. By assumption, we only consider heat exchange mechanisms that are linear in the temperature difference, thus neglecting any radiative effects. Given this assumption, a lumped-capacitance/equivalent thermal circuit approach (see Section 5.3 of [41]) is employed by which the battery pack

[5]The choice of using accumulated discharge-energy throughput in the aging models is motivated by the available experimental data although it differs from previous works (e.g. [20], [29], [40]) where aging models are based on ampere-hour throughput. Nevertheless, the battery's discharge energy throughput provides a metric for the accumulated usage of the battery. As such, we use it here to characterize the capacity fade and HFR increase observed.

[6]Simscape is an extension of MATLAB's Simulink graphical environment that is geared towards the modeling of multi-domain physical systems. In particular, connections between electrical elements in this environment automatically impose Kirchoff's current and voltage laws.

enclosure is modeled as a thermal mass characterized by a heat capacity C_{pack} and whose temperature evolves as

$$C_{\text{pack}}\frac{\mathrm{d}}{\mathrm{d}t}T_{\text{pack}}(t) = \frac{1}{R_{\text{d}}}\left[T_{\text{amb}} - T_{\text{pack}}(t)\right] + \frac{1}{R_{\text{pm}}}\sum_{q=1}^{48}\left[T^{(q)}_{\text{module}}(t) - T_{\text{pack}}(t)\right] . \tag{13}$$

The first term on the RHS of (13) represents the thermal exchange between the pack enclosure and the ambient air temperature mediated by the thermal resistance R_{d}[7]. The second term represents the thermal exchange between the battery modules contained within the battery pack mediated by the thermal resistance R_{pm}.

Each battery module $m \in \{1, \cdots, 48\}$ within the pack is modeled as a thermal mass characterized by a heat capacity C_{module}. The temperature dynamics of a module are described according to the scenarios described below:

- Scenario 1: if the mth battery module in the pack has two nearest neighbors, $m-1$ and $m+1$, then its lumped thermal dynamics are as follows:

$$C_{\text{module}}\frac{\mathrm{d}}{\mathrm{d}t}T^{(m)}_{\text{module}}(t) = \frac{1}{R_{\text{pm}}}\left[T_{\text{pack}}(t) - T^{(m)}_{\text{module}}(t)\right] + \frac{1}{R_{\text{mm}}}\left[T^{(m-1)}_{\text{module}}(t) - T^{(m)}_{\text{module}}(t)\right] + \frac{1}{R_{\text{mm}}}\left[T^{(m+1)}_{\text{module}}(t) - T^{(m)}_{\text{module}}(t)\right] + \frac{1}{R_{\text{mc}}}\sum_{c\in m}\left[T^{(c)}_{\text{cell}}(t) - T^{(m)}_{\text{module}}(t)\right] \tag{14}$$

- Scenario 2: if a module has only one nearest neighbor n then its lumped thermal dynamics are:

$$C_{\text{module}}\frac{\mathrm{d}}{\mathrm{d}t}T^{(m)}_{\text{module}}(t) = \frac{1}{R_{\text{pm}}}\left[T_{\text{pack}}(t) - T^{(m)}_{\text{module}}(t)\right] + \frac{1}{R_{\text{mm}}}\left[T^{(n)}_{\text{module}}(t) - T^{(m)}_{\text{module}}(t)\right] + \sum_{c\in m}\frac{1}{R_{\text{mc}}}\left[T^{(c)}_{\text{cell}}(t) - T^{(m)}_{\text{module}}(t)\right] \tag{15}$$

The first term on the RHS of (14) and (15) represents the exchange of heat between the module and the pack. The last term represents the heat contribution of all the cells c enclosed by the mth module. The second term, in (14) and (15), and third term, in (14), model the exchange of heat between the mth module and its nearest neighbors. We emphasize that the topology of the electrical circuit of all the modules need not be directly related to the topology of the thermal circuit of all the modules and the pack enclosure.

The temperature $T^{(i)}_{\text{cell}}$ of each cell i in the mth module

[7]The thermal resistances considered in this work encapsulates the net effect of both convection and conduction heat exchange mechanisms.

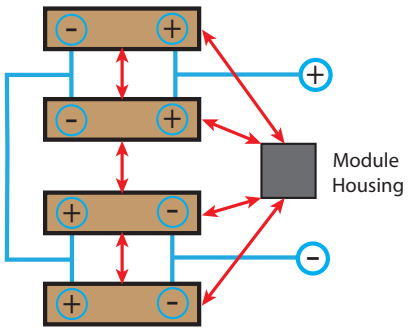

Fig. 3: ***Battery module configuration.*** *Cells are electrically connected in a 2P2S configuration. Spatially, the cells are stacked on top of one another. Each cell exchanges heat (denoted by the red bi-directional arrows) with its nearest neighbors and the module housing.*

evolves according to,

$$C_{\text{cell}}\frac{\mathrm{d}}{\mathrm{d}t}T^{(i)}_{\text{cell}} = I^{(i)}_{\text{cell}}(t)\left[V^{(i)}_{\text{oc}}\left(\text{SoC}^{(i)}\right) - V^{(i)}_{\text{cell}}(t)\right] + \frac{1}{R_{\text{mm}}}\left[T^{(m)}_{\text{module}}(t) - T^{(i)}_{\text{cell}}(t)\right] + \frac{1}{R_{\text{cc}}}\left[T^{(i-1)}_{\text{cell}}(t) - T^{(i)}_{\text{cell}}(t)\right] + \frac{1}{R_{\text{cc}}}\left[T^{(i+1)}_{\text{cell}}(t) - T^{(i)}_{\text{cell}}(t)\right] , \tag{16}$$

where the second-term on the RHS represents the thermal exchange between the cell and the module enclosure while the third and fourth terms represent the nearest-neighbor heat exchange between cells. The battery cells, their electrical connections, and their thermal (heat exchange) interaction with each other and the module housing are schematically shown in Fig. 3. We note that, similar to some modules, there are also cells within a given module that only have one nearest neighbor (e.g., the top- and bottom-most cells shown in Fig. 3). For these cells, we remove either the third or fourth term on the RHS of (16) as appropriate. In summary, the pack model thermal parameters are R_{d}, R_{pm}, R_{mm}, R_{mc}, $R_{\text{mc}}, C_{\text{module}}, C_{\text{pack}}$[8]. These parameters are calibrated with experimental data for a fresh pack as described in Appendix C.

B. Battery Pack Model Validation

Having constructed the battery pack as described in Section IV-A, and calibrated the pack as in Appendix C, the fresh pack model voltage and temperature outputs are validated in this section. Assuming that the fresh pack contains no cell-to-cell variations, the pack model is tested with the input dynamic profile shown in Fig. 4a and the model outputs of pack voltage and pack temperature are compared with the experimentally collected data. The experimental data is obtained from the second drive cycle in the second month of the experiment[9]

[8]In principle, each of the thermal resistances could be different for every pair of cells/modules in the pack. For parsimony, here we assume that each of the thermal resistances holds a specific value for all pairs of cells/modules in the pack.

[9]Problems with the drive cycle converter current limiting the high power steps occurred in the first month and the test was stopped temporarily as the profiles were re-generated. For simplicity, the model is calibrated using the second month of experimental data.

in Fig. 4. We find that the voltage output of the battery pack model agrees well with the experimental data with a voltage RMSPE of 0.51%. The error metrics used for cells, defined in (25) and (26), are also used for the pack. We hypothesize that the discrepancy between the model's output voltage and the experimental data at the end of the charge period, comes from not modeling the passive balancing circuits present within the pack during charging[10].

To obtain the pack temperature, the experimental readings from four thermocouples attached to specific locations in the pack (see Fig. 1, red points, roman numeral identifiers for locations) are averaged and the resulting signal is smoothed using a Savitzky-Golay filter. The average module temperature of the model, obtained by averaging over all the module temperatures, also finds good agreement with the experimental data with a temperature RMSPE of 0.73%.

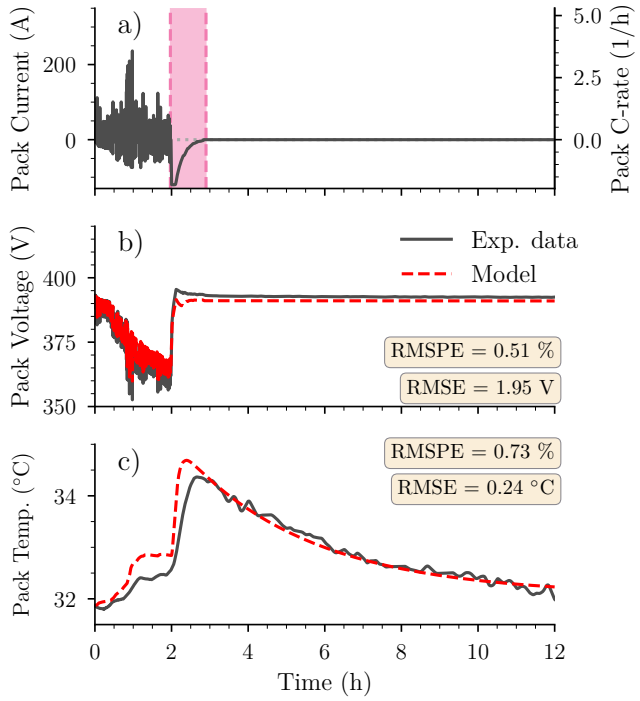

Fig. 4: ***Battery pack model validation.*** *a) Dynamic input current profile based on Nissan Leaf data is used in the battery pack simulations. The constant-current constant-voltage charge portion is (shaded pink region) followed by a long rest period. b) Experimental voltage measurements (solid black curve) under the dynamic current profile in a) is compared against the model output voltage from the calibrated battery pack model (dashed red curve). c) Experimental pack temperature readings obtained from averaging the data of 4 thermocouples located within the pack (solid black curve) compared against the model module temperature prediction from the calibrated battery pack model (dashed red curve).*

V. Case Study 1: Normally-Distributed Initial Cell-to-Cell Capacity Variation

Having validated the cell and pack models, we now use the fresh pack model to study the effects of cell-to-cell capacity variation on the voltage response of the pack, the temperature response of the modules, and the properties of the cells. Specifically, in this section, we consider a pack where all the cells have initial capacities drawn from a normal distribution,

$$Q^{(i)}(t=0) \sim \mathcal{N}\left(Q^{(i)}; \mu = Q_{\text{nom}}, \Sigma_Q^{\text{initial}}\right) \ , \tag{17}$$

with mean fixed to the nominal rated capacity $Q_{\text{nom}} = 33.1$ Ah and with a variable standard deviation $\Sigma_Q^{\text{initial}} \in [10^{-4}, 1]$ Ah, [42]. We compare the outputs of this pack model, with the outputs of a pack model which does not have an initial cell-to-cell capacity variation.

A. Comparison of pack and module dynamics

We first compare the pack voltage $V_{\text{pack}}^{\text{var}}(t)$ and module temperature $T_{\text{module}}^{\text{var}}(t)$ output of a pack with $\Sigma_Q^{\text{initial}} > 0$ (see (17)) against the pack voltage $V_{\text{pack}}^{\text{nom}}(t)$ and module temperature $T_{\text{module}}^{\text{nom}}(t)$ outputs of a pack with $\Sigma_Q^{\text{initial}} = 0$[11]. We stress that, even for the pack with no initial capacity variation, there is still heat exchange between the cells and modules of the pack. We compute the difference between the voltage and module temperature time series,

$$\Delta V_{\text{pack}}(t) = V_{\text{pack}}^{\text{var}}(t) - V_{\text{pack}}^{\text{nom}}(t) \tag{18a}$$

$$\Delta T_{\text{module}}(t) = T_{\text{module}}^{\text{var}}(t) - T_{\text{module}}^{\text{nom}}(t) \ , \tag{18b}$$

and analyze the distribution of these differences as a function of the initial capacity variation $\Sigma_Q^{\text{initial}}$. We see, in Fig. 5, that the introduction of an initial capacity variation does introduce small differences in the pack's voltage and temperature. The voltage is, on average, higher for a fresh pack with cell-to-cell capacity variation (Fig. 5a). Conversely, the module temperatures are, on average, relatively similar with $\mu_{\Delta T_{\text{module}}} \approx 0$ until the variation becomes sufficiently large, $\Sigma_Q^{\text{initial}} > 0.1$ Ah. In addition, the introduction of capacity variations results in a monotonic increase in the relative spread of temperature values, $\Sigma_{\Delta T_{\text{module}}}^{\text{final}}$, experienced by the cells of the pack (Fig. 5b and right-axis inset). Such an inhomogeneity of temperatures would likely be exacerbated upon repeated use of the battery resulting in an acceleration of aging.

B. Propagation in cell-level quantities

In this section, we look to see how cell-to-cell capacity variation (17) affects other electrical quantities, particularly the distribution of capacity $Q^{(i),\text{final}}$, the final $\text{SoC}^{(i),\text{final}}$, and the HFR $R_0^{(i),\text{final}}$, after the application of a 7088s drive cycle (Fig. 4a).

Interestingly, we observe (Fig. 6a) that, averaging over different values of $\Sigma_Q^{\text{initial}}$, the ratio of standard deviations between the final and the initial capacity distributions is $\Sigma_Q^{\text{final}}/\Sigma_Q^{\text{initial}} \approx 0.92$. This indicates that the degree of cell-to-cell variation decreases after the application of a drive cycle profile and is consistent with findings from previous studies [43].

[10]During the experiment [10], the BMS and balancing circuits were active and thus any additional heat contributions of these circuits is not captured by our model.

[11]The superscripts "var" and "nom" differentiate the quantities as being associated with either a pack with cell-to-cell **var**iation or a pack with all **nom**inal cells, respectively.

This article has been accepted for publication in IEEE Transactions on Transportation Electrification. This is the author's version which has not been fully edited and content may change prior to final publication. Citation information: DOI 10.1109/TTE.2024.3365028

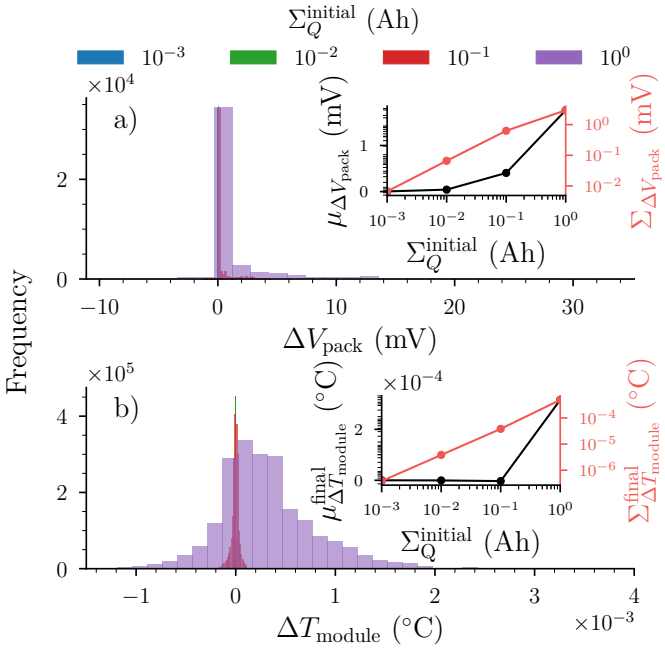

Fig. 5: ***Introduction of capacity variation, in the form of (17), results in small differences in the pack voltage and module temperatures within the pack.*** *Each plot shows a quantity after the application of the full input current profile in Fig. 4a at $T_{\text{amb}} = 30$ °C, for different values of the initial capacity standard deviation $\Sigma_Q^{\text{initial}}$. a) Distribution of differences in pack voltage between a pack (18a) with initial capacity variation and without. b) Distribution of differences in module temperatures (18b) for all modules in the pack. Insets: the mean (left axis) and the standard deviation (right axis) for each of the distributions shown as a function of the initial capacity standard deviation.*

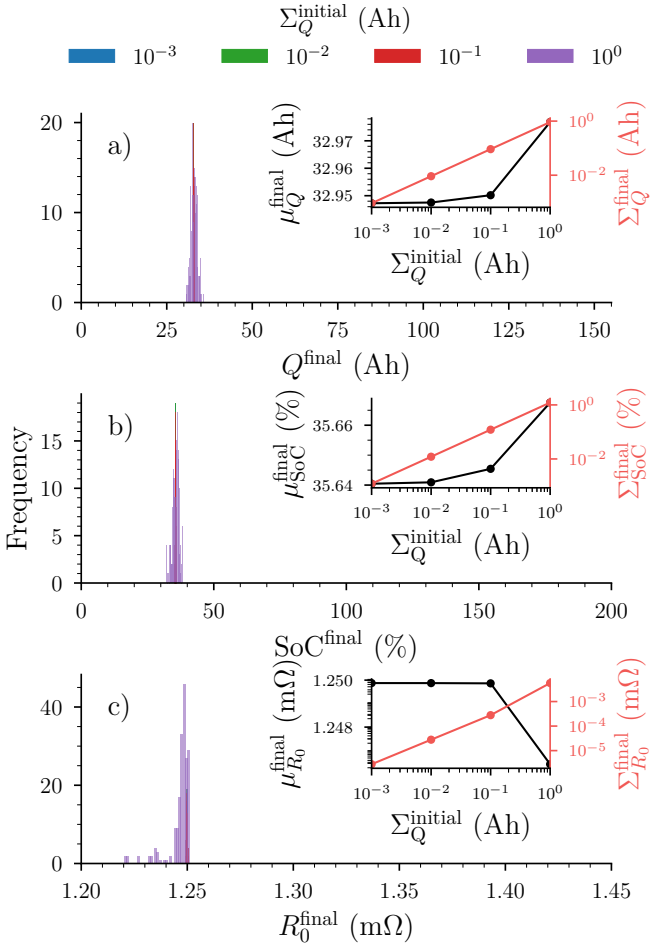

Fig. 6: ***Effect of initial capacity variation on the final cell capacity, SoC and the high-frequency resistance.*** *Each plot shows the distribution of cell quantities after the application of the 7088s drive cycle input shown in Fig. 4 for different values of the initial capacity standard deviation $\Sigma_Q^{\text{initial}}$. a) Distribution of capacities Q^{final} of all the cells in the pack. b) Distribution of state-of-charge $\text{SoC}^{\text{final}}$ of all the cells in the pack. c) Distribution of high-frequency resistance R_0^{final} of all the cells in the pack. Insets: the mean (left axis) and the standard deviation (right axis) for each of the distributions shown as a function of the initial capacity standard deviation.*

Introduction of capacity variation will invariably introduces variation in the SoC of the cells in the pack (Fig. 6) since SoC depends on the capacity (3). For simplicity, we assume that the SoC of all the cells in the pack, prior to the application of the dynamic current profile, are the same, i.e., $\text{SoC}^{(i)}(t = 0) = 95\%\ \forall\ i$. After the application of the drive cycle profile, we see (Fig. 6b) that the standard deviation of the distribution of the SoCs $\Sigma_{\text{SoC}}^{\text{final}}$, follows a similar trend to that of the standard deviation of the capacities, suggesting that the initial variation in the cells' capacities propagated directly to the cells' SoCs.

It is shown the distribution of SoC values also affects the electric parameters. Specifically, we focus our attention on its effect on the HFR R_0 where all cells have the same initial HFR value. Figure 6c shows that, after applying the drive cycle profile, the distribution of SoC values also results in the cells of the pack having a distribution of HFR values with a standard deviation $\Sigma_{R_0}^{\text{final}}$ that grows monotonically with the initial capacity standard deviation. However, the variation introduced in the SoC and the HFR, as measured by the standard deviation, is much less than the variation that is introduced into the capacity initially, $\Sigma_{R_0}^{\text{final}} \ll \Sigma_Q^{\text{initial}}$.

VI. Case Study 2: Introducing Cells with Deliberately Lowered Capacity into the Pack

As a second application of the battery pack model, we explore how the energy utilization of the pack changes when we insert cells with reduced capacity as a function of the number of these cells.

A. Comparison of energy utilization between ideal and realistic pack models

We investigate the effects of cell-to-cell variations in the battery pack upon introducing cells of lower capacity as a function of the number of such cells. These lower capacity cells are equivalent in all other parameters to their nominal capacity counterparts but have their capacities reduced by a percentage $p \in \{5, 10, 20, 40\}$ %. For ease of discussion, we refer to these lower capacity cells as "weak cells" while the cells with nominal capacity are referred to as "normal cells". Correspondingly, a pack containing weak cells is referred to as a "weak pack" while a pack with only normal cells is referred to as a "normal pack". From a pack model where all 192 cells are normal cells, a number N_{weak} of these cells are uniformly randomly picked to replace with weak cells.

This article has been accepted for publication in IEEE Transactions on Transportation Electrification. This is the author's version which has not been fully edited and content may change prior to final publication. Citation information: DOI 10.1109/TTE.2024.3365028

We examine how the pack energy utilization ($I_{\text{pack}} \in \mathbb{R}$),

$$E(t) = \int_0^{\tau} |I_{\text{pack}}(t) V_{\text{pack}}(t)| \, \mathrm{d}t \ , \tag{19}$$

during the application of the drive cycle (Fig. 4) changes as a function of p and N_{weak} compared to the pack energy utilization obtained from the ideal pack model (1). The total duration of the drive cycle is denoted by τ which here is equal to 7088 s. Figure 7 shows the relative difference in energy delivered by the ideal pack relative to a realistic pack at a particular time t,

$$E_{\text{reduced}}(t) = 100 \times \left(1 - \frac{E^{\text{ideal}}(t)}{E^{\text{realistic}}(t)}\right) \ , \tag{20}$$

where the number of weak cells N_{weak} and capacity reduction percentage p are varied and the energy utilization of an ideal and realistic pack are denoted by $E^{\text{ideal}}(t)$ and $E^{\text{realistic}}(t)$, respectively. In particular, Fig. 7a compares the ideal pack to a normal pack (i.e., a realistic pack containing only normal cells). We find that the relative difference in the energy output of both packs remains within 1% throughout the 7088 drive cycle[12], although the ideal pack consistently overestimates the amount of energy delivered. As we increase the number of weak cells in the pack, from $N_{\text{weak}} = 0$ to $N_{\text{weak}} = 39$ (Figs. 7b-d) we see that the relative difference of the pack energy utilization between both packs remains within one percent. The simulations suggest that the pack energy utilization is relatively insensitive to the additional details that are included in the realistic model but that are neglected in the ideal model. Thus, the use of the ideal model to estimate the energy needs of vehicles (among other applications) is justified.

While we have simulated a battery pack with cells that have lost up to 40% of their rated capacity, we emphasize that such cases would be rare for battery packs deployed in EVs that are controlled by a battery management system (BMS) [44], as the BMS will trigger a warning to alert the user that maintenance is needed [45] when the maximum voltage difference between the cells is greater than 10% of the difference between the cell's high and low voltage limits, which here is $\Delta V_{\text{max}} = 160$ mV (dotted line, Fig. 7 insets).

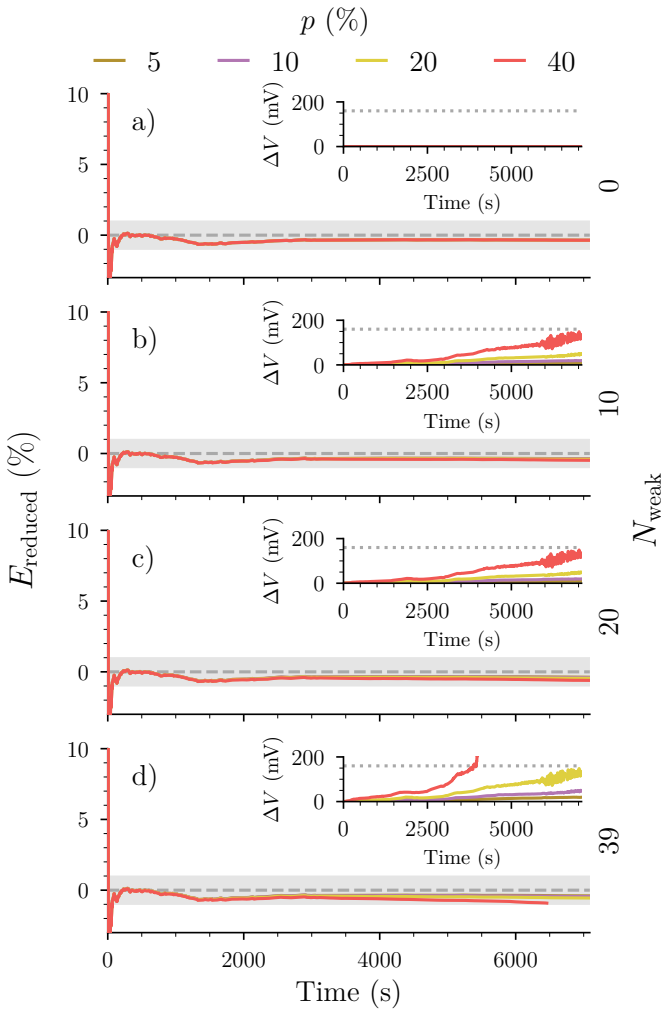

Fig. 7: ***The relative difference in energy utilization between an ideal and realistic pack model is over one driving cycle.*** *Each plot shows the percent decrease in energy delivered by a pack with weak cells compared to an ideal pack (1) as a function of time for the 7088s drive cycle shown in Fig. 4a. The number of weak cells introduced to the pack increases going down the rows (a to d). The orange curve in d) stops just before 6400s as the battery pack reaches 0% SoC. Different colors within a given plot denote different percent of capacity reduction p. Dashed gray line: 0% change in energy. Shaded region: ± 1% change in energy delivered. Insets: the voltage difference between the maximum and minimum voltage cells. Inset dotted gray line: 10% voltage difference BMS alert limit.*

B. Self-balancing effects at the battery cell-level

To explore how the battery pack energy remains resilient to cell-to-cell variations, as we see in Section VI-A, we examine the cell-by-cell energy utilization difference between a weak pack and a normal pack. A weak pack is chosen where $N_{\text{weak}} = 39$ and with $p = 20\%$ percentage capacity reduction. We focus on the first 20 cells (i.e. Modules 1-5, see Fig. 1) in the pack for ease of presentation: The behaviors seen in these modules are representative of the other modules in the pack. In these first twenty cells, we see a total of four weak cells with indexes 1, 11, 17, and 18; the rest of the cells are normal. The weak cells 1 and 11 are in parallel pairs[13] with normal neighbors while cells 17 and 18 form a parallel pair where both cells are weak. This is an extreme case of initial capacity variation but clearly illustrates the effects of these weaker cells on their neighbors. Here, we use a "modified drive cycle" that is constructed by taking the pack current profile shown in Fig. 4a, truncating this profile to the first 15,000 seconds, and applying this truncated pack current profile sequentially three times to the weak and normal pack.

We compute for each cell, the energy difference between the

[12]The large values of $\Delta E > 1\%$ observed in during the first 60 s of the drive cycle in Fig. 7 is due to the energy values initially being small for both ideal and realistic packs. Notably, the absolute difference between the energy output of the ideal and realistic pack is small at the beginning of the drive cycle (approx. 1 Wh) even if the relative difference is large ($> 10\%$).

[13]A "parallel pair" is defined here as two cells connected in parallel together. Each battery module contains 2 parallel pairs. For example, in module 1 of the pack, cells 1 and 2 form a parallel pair, and cells 3 and 4 form another parallel pair. There are a total of 96 such pairs in the entire battery pack.

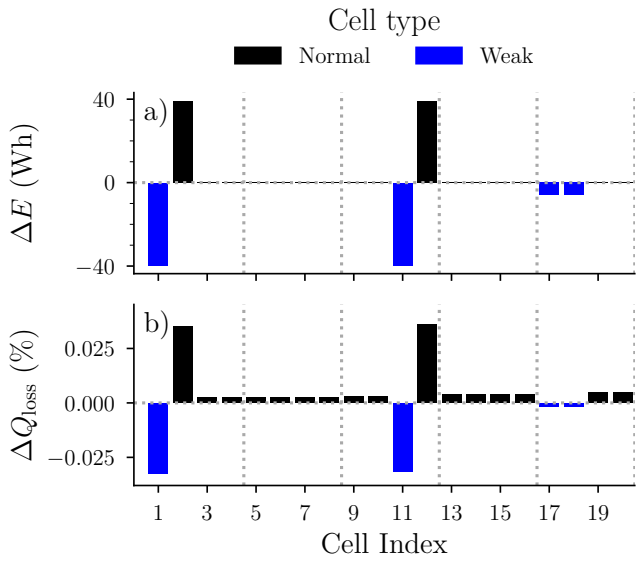

Fig. 8: ***Parallel-connected cells can self-balance at the expense of increased aging.*** *a) Difference of energy-throughput between cells in a weak pack and cells in a normal pack. b) Difference in capacity fade between the cells in a weak pack and cells in a normal pack. Weak cells (reduced capacity) are shown in blue. Cells with nominal capacity are shown in black. The gray dashed vertical lines demarcate which cells are grouped together in a single module with a 2P2S (4 cells/module) configuration. Subsequent numbers are paired together in a parallel pair.*

total energy-throughput (19), where here τ is equal to 45,000 s, of cells in a weak pack, $E^{(i)}_{\text{weak}}$, and the cells in a normal pack $E^{(i)}_{\text{norm}}$:

$$\Delta E^{(i)} = E^{(i)}_{\text{weak}} - E^{(i)}_{\text{norm}} \ . \tag{21}$$

We see in Fig. 8a that for parallel pair where one of the cells is weak (e.g. cells 1 & 2), the stronger of the two cells takes on a greater amount of energy-throughput than it otherwise would if both of the cells in the branch were normal. In this particular case, the stronger cell discharges $\approx$ 40 Wh *more* energy compared to the normal case; symmetrically, the weaker cell discharges $\approx$ 40 Wh less energy. This "self-balancing" behavior is seen in other works that have investigated parallel-connected cells [43]. Thus, we see that weak cells with a normal partner on the same parallel branch, can be balanced by its parallel-connected partner thereby mitigating the effect of cell-to-cell variation.

While this self-balancing effect is beneficial, in that the effect of the capacity variation on the short-term pack output energy is small, long-term it can be overall detrimental to the cells in the pack as bearing higher loads generally also implies a greater amount of aging. To quantify this, the cell capacity aging model, (9) and (10), is used to compute the difference,

$$\Delta Q^{(i)}_{\text{loss}} = Q^{(i)}_{\text{loss,weak}} - Q^{(i)}_{\text{loss,norm}} \ , \tag{22}$$

between the fraction of capacity remaining in the cells of a weak pack,

$$Q^{(i)}_{\text{loss,weak}} = \frac{Q^{(i)}_{\text{initial,weak}} - Q^{(i)}_{\text{final,weak}}}{Q^{(i)}_{\text{initial,weak}}} \tag{23}$$

to the fraction of capacity remaining in the cells of a normal pack,

$$Q^{(i)}_{\text{loss,norm}} = \frac{Q^{(i)}_{\text{initial,norm}} - Q^{(i)}_{\text{final,norm}}}{Q^{(i)}_{\text{initial,norm}}} \ , \tag{24}$$

after application of the modified drive cycle. A positive value of (22) implies a greater amount of aging for a cell i in a weak pack, relative to the amount of aging the same cell experiences in a normal pack. We see (Fig. 8c) that the cells which bear a higher energy-throughput due to having a weak partner experience a significant amount of aging relative to the aging they would experience in a normal pack. Conversely, the weaker cells do not age as much as they would have in a normal pack. This increase in the aging of the normal cells and simultaneous decrease in the aging of the weak cells, relative to their aging if in a normal pack, explains the reduction in the standard deviation in the final capacity distribution relative to the initial capacity distribution seen in Section V-B (Fig. 6a). Moreover, we also observe in Fig. 8 that the other normal cells in the weak pack without weak partners have aged more than they would have if they were in a normal pack. This suggests that the initial variation in cell-to-cell capacity results in an overall increased aging rate of the pack. We emphasize that these findings are generated by our model and not a direct experimental finding. Nevertheless, while this type of capacity variation has not been considered previously, these results are consistent with the findings of previous models [31], [32].

VII. Conclusions

In this article, we have constructed a battery pack model based on data from cells and the pack of a first-generation Nissan Leaf. We use experimental data to calibrate and validate the models, both at cell and pack levels. The pack model is used to investigate the effects of cell-to-cell variation at the pack level, as well as how this variation changes the dynamics of individual cells. Variations between the cells of a battery pack generally arise due to small differences during cell manufacturing process or it could arise due to inhomogeneous aging of cells in the pack throughout its lifetime.

Capacity variations are found to affect the cells' SoCs as well as their high-frequency resistance. Despite the introduction of this cell-to-cell variation, we observe that, unless the variation is particularly severe, within a single application of a dynamic drive cycle, the effect of these variations on the pack voltage and module temperatures is relatively small; however, these small differences can be exacerbated upon repeated application of drive cycles.

In addition, we find that the pack energy utilization is relatively insensitive to cell-to-cell capacity variation, as we see when we deliberately introduced lower-than-nominal capacity cells into a our realistic pack model and compare it to the pack energy utilization of an ideal pack. This might be due the ability of parallel-connected cells to "self-balance". Specifically, if a cell with lower-than-nominal capacity is connected in parallel to a cell with nominal capacity, this lower-than-nominal capacity cell be accommodated by having the nominal capacity cell bear a larger energy load. On the

other hand, this increase in load (energy) borne by the nominal capacity cells increases the rate of aging for these cells in a given drive cycle. As such, the "self-balancing" effect of cells in parallel comes at the cost of increased aging for the pack overall. Given the results from our simulations, the ideal pack model is a reasonable approximation for battery packs with parallel-connected cells, as the "self-balancing" effect is able to reduce the effects of cell-to-cell variation. This is particularly true if one cares most about estimating the energy utilization of a vehicle/truck, as we see that energy utilization is relatively insensitive to cell-to-cell variation for packs with parallel-connected cells. Contrarily, if one cares to estimate the aging of a battery pack, greater care must be taken to account for cell-to-cell variation effects and the heat exchange between the cells especially since, as we have seen, these can lead to a greater degree of aging for the pack overall.

Since this work uses empirical models, the fidelity of these are limited by the scope of the data that is used to calibrate them. More data at both the cell and the pack level that cover a wider range of conditions would allow for the construction of more accurate pack models. Furthermore, we have constructed the battery pack model based on the configuration of a Nissan Leaf battery pack. While some general principles can be gleaned from the battery pack construction framework we present here, it is important to note that the specific model we constructed will not directly generalize to other battery packs.

ACKNOWLEDGMENT

The authors thank Dr. Maitri Uppaluri, Dr. Le Xu and Luigi Tresca (Energy Sciences and Engineering, Stanford U.) for their feedback on the manuscript. Experimental data used in this work was provided by Dr. Eric Dufek and Mr. Matthew Shirk (Idaho National Lab). This work is part of Lab Call Project L096-1568 in partnership with The Ohio State University and Oak Ridge National Lab. Funding for this project is provided by the Vehicles Technologies Office (VTO). J.N.E.L. gratefully recognizes additional support from the National Sciences and Engineering Research Council of Canada's Postgraduate Scholarships – Doctoral Award (PGS-D). This research is enabled in part through computational resources and support provided by Sherlock compute cluster @ Stanford University (https://www.sherlock.stanford.edu)

APPENDIX A
BATTERY CELL SUB MODEL CALIBRATION

In this section, we detail how the electric, thermal, and aging submodels of the battery cell are calibrated.

To calibrate the battery cell electric model, we follow the procedure detailed in [17], using experimental hybrid power pulse characterization (HPPC) voltage data from [10], where the objective is to minimize the percentage root-mean-square error,

$$\mathrm{RMSPE}(\theta) = 100 \times \sqrt{\frac{1}{N_{\mathrm{meas}}} \sum_{k=1}^{N_{\mathrm{meas}}} \left(1 - \frac{\mathcal{O}_r^{\mathrm{model}}[k;\theta]}{\mathcal{O}_r^{\mathrm{exp}}[k;\theta]}\right)^2}, \tag{25}$$

between the experimentally measured signal $\mathcal{O}_r^{\mathrm{exp}}$ and the model prediction $\mathcal{O}_r^{\mathrm{model}}$ with respect to the model parameters θ. Here, r distinguishes between the voltage and temperature signals. To perform the optimization, the Particle Swarm Optimization (PSO) algorithm is used (see Section 9.4 of [46]). A given experimental signal is collected at a sampling frequency of f_{s} for a total time of T_{tot} leading to a total number of samples, $N_{\mathrm{meas}} = f_{\mathrm{s}} \cdot T_{\mathrm{tot}}$. For the HPPC experiment, the sampling frequency is set to $f_{\mathrm{s}} = 10$ Hz and the total time of the experiment was $T_{\mathrm{tot}} \approx 11.5$ hrs. The maximum discharge C-rate experienced by the cell during the HPPC test is 1C. The identification error is quantified by the root-mean-square error

$$\mathrm{RMSE}(\theta) = \sqrt{\frac{1}{N_{\mathrm{meas}}} \sum_{k=1}^{N_{\mathrm{meas}}} \left(\mathcal{O}_r^{\mathrm{exp}}[k;\theta] - \mathcal{O}_r^{\mathrm{model}}[k;\theta]\right)^2}, \tag{26}$$

The results of this calibration, over three different temperatures and three different replicate cells at each temperature, are shown in Fig. 9. We pick "Cell 3" as our representative cell[14]

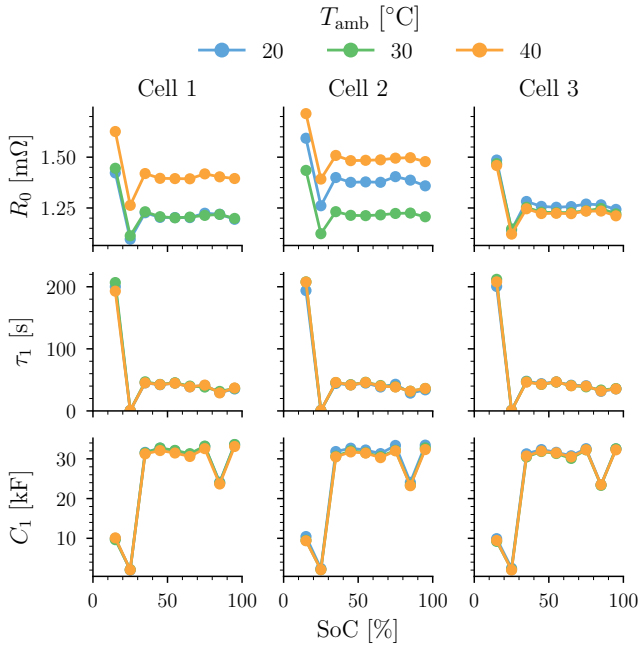

Fig. 9: ***Calibrated parameters for fresh cells as a function of SoC and temperature for the three cells within the dataset.*** *The ECM parameters, R_0, τ_1, and C_1, are shown in the rows. Calibrated electrical parameters for the three different cells are shown in the different columns. Different colors denote different ambient temperature conditions.*

and use the parameters obtained for this cell in the battery pack analysis.

A representative calibration result ($T_{\mathrm{amb}} = 30°\mathrm{C}$) of the ECM and thermal model to HPPC data is shown in Fig. 10. An RMSE of 3% and 0.24% for the voltage and temperature,

[14]We were informed through private correspondence with the authors of [10], that the voltage sense leads of cells 1 and 2 had higher than expected internal resistance values for the first 3 months of measurements. As such, we base our analysis on cell 3 parameters to avoid any potential issues arising from the problem with the leads.

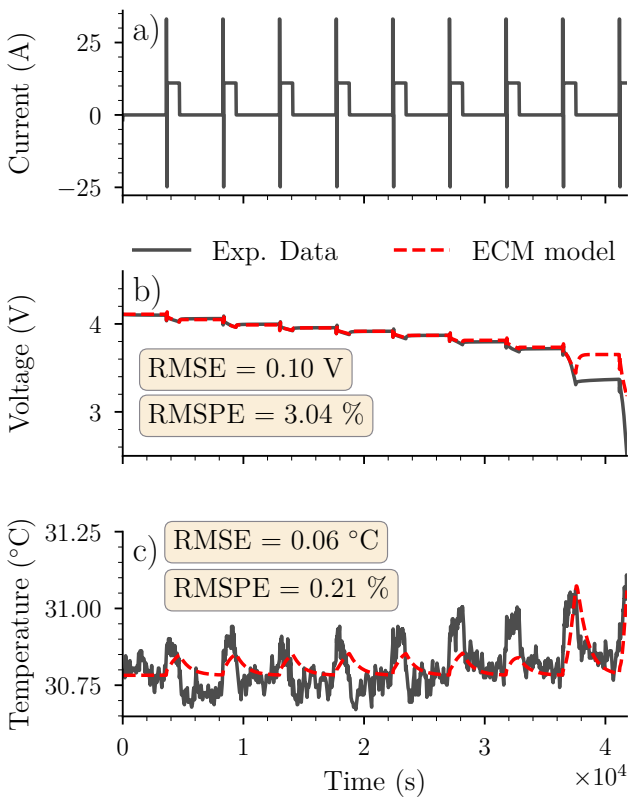

Fig. 10: ***Cell voltage and temperature model performance.*** *a) Input HPPC current profile. b) Voltage comparison between experimental data (black solid curve) and model output (dashed red curve). c) Temperature comparison. The ambient temperature for the HPPC test shown is set to* $T_{\text{amb}} = 30\ ^\circ\text{C}$.

respectively, is obtained. The agreement, however, is noticeably poorer at low SoCs. This is likely caused by inaccuracy of the $V_{\text{oc}}(\text{SoC})$ relation, used in the output equation of ECM model (2b), obtained from a $C/3$ discharge experiment. We see in Fig. 11 that, comparing the pseudo-OCV vs. SoC relationship obtained from a C/3 capacity test to the OCV vs. SoC obtained by measuring the battery voltage at the end of each rest period in an HPPC test (Fig. 10b), there is a marked difference between the two OCV estimates at lower ($< 25\%$) SoCs. The calibration of the battery cell

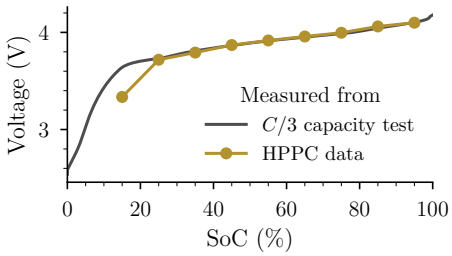

Fig. 11: Comparison between the voltage from $C/3$ *discharge (used as OCV in the cell model) and the OCV from HPPC, interpolating the OCV readings at resting time, done on the same cell at ambient temperature* $T_{\text{amb}} = 30^\circ\text{C}$.

thermal model follows exactly the same procedure, using the associated HPPC temperature data. From this calibration, the cell thermal parameters are optimized and the values of $C_{\text{cell}} = 2.9\ \text{kJ/K}$ and $R_{\text{mc}} = 0.3\ \text{kJ/K}$ are obtained. By assumption, the thermal parameters are independent of aging[15].

To calibrate the semi-empirical aging models, we follow the procedure first proposed in [20]. For concreteness, we outline here the calibration procedure for the capacity fade model, composed of three steps: (1) assuming the capacity loss model $Q_{\text{loss}} = \sigma_Q \cdot \text{Wh}_{\text{dchg}}^{\zeta_Q}$, a nonlinear least-squares problem, varying the exponent value ζ_Q, is formulated to minimize the difference between the experimental capacity fade data and the capacity loss model output. Fixing the exponent value ζ_Q to its optimally found value from the previous step, (2) the severity factor values σ_Q corresponding to the optimal ζ_Q are obtained. Given the severity factor function values, (3) the parameters of the severity factor function σ_Q are calculated using nonlinear least-squares. This is done separately for the capacity fade and HFR increase aging models.

To calibrate the capacity fade model (9), we use experimental capacity data obtained from $C/3$ capacity tests performed at every month (11 capacity measurements total) of the experiment. To quantify the error of the overall fit, we evaluate the mean-square error (MSE) between the experimental data and the model prediction averaged over the capacity fade measurements obtained from each month of the experiment,

$$\begin{aligned} &\text{MSE}_{T_{\text{cell}}}(\zeta_Q) \qquad (27)\\ &= \frac{1}{11}\sum_{k=1}^{11}\left(Q_{\text{loss}}^{\text{model}}[k,\zeta_Q,T_{\text{cell}}] - Q_{\text{loss}}^{\text{exp}}[k;\zeta_Q,T_{\text{cell}}]\right)^2 , \end{aligned}$$

for a fixed value of the exponent ζ_Q. The square root of the average (over the 3 temperatures) of the MSE values is computed and an average RMSE,

$$\overline{\text{RMSE}} = \sqrt{\frac{1}{3}\sum_{m=1}^{3}\text{MSE}_m(\zeta_Q)}\ , \qquad (28)$$

is obtained, which we use as our calibration metric in Figs. 12, 13, and 15.

We show the results of the calibration in Fig. 12. From these, we observe the exponent of $\zeta_Q = 0.5$ yields the best fit to data and this value is used for the remainder of the calibration. Fixing the value of the exponent to $\zeta_Q = 0.5$ and we obtain a set of severity factor values. We then fit the severity factor function (10) to these values and obtain the following parameters: $\alpha_Q = 3.78782 \times 10^3$ K, and $\gamma_Q = 1.16872 \times 10^4$. The comparison of the calibrated capacity fade aging model (9) output to experimental data is shown in Fig. 13. Following a similar calibration procedure to the capacity fade aging model, the HFR increase aging model is identified using HFR values obtained by calibrating a different ECM model (as a function of temperature and SoC) to the HPPC data obtained during each month of the experiment, under the assumption that the other parameters of the ECM, τ_1 and C_1, do not change with aging. We find that an exponent value of $\zeta_{R_0} = 1.05$ in (11) yields the best fit

[15]The thermal parameters could also be different for each cell in the pack. In this work, we only consider the case where these parameters are the same for all cells in the pack.

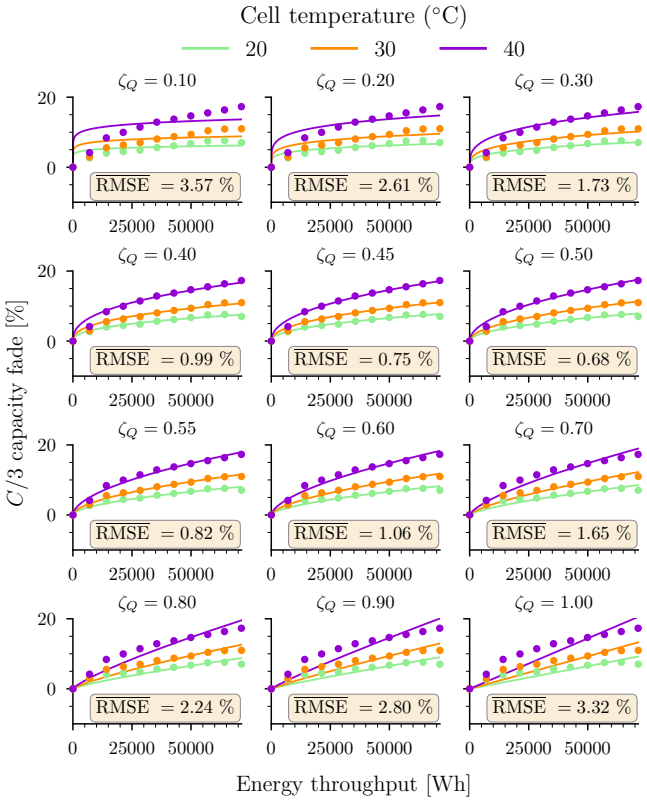

Fig. 12: ***Identification of ζ_Q in the cell capacity fade aging model*** *(9). Each plot corresponds to a different value of the exponent ζ_Q. The capacity fade aging model calibrated at a fixed exponent value (solid curves) is shown against the experimental capacity fade data (circle markers). Different colors denote different cell temperatures. The average root-mean-square error $\overline{RMSE}$ is defined in (28).*

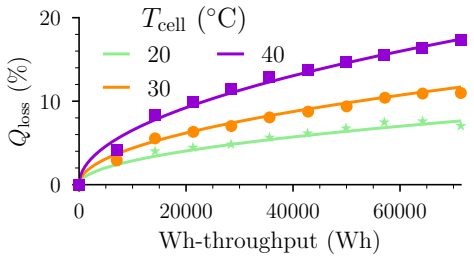

Fig. 13: ***Cell capacity fade aging model fit to data****. a) Capacity fade severity factor function model (10) (blue solid curve) calibrated to the values obtained from the experimental data best curve fittings (black points) as a function of cell temperature. b) Capacity fade based on C/3 capacity test. Points denote experimental data obtained from [10, Fig. 3]. Solid lines show the predictions of the calibrated capacity fade model (9). The calibrated models for 20°C, 30°C, and 40°C attain an RMSE of 0.39%, 0.39%, and 0.5%, respectively. Different colors denote data for different cell temperatures.*

to the obtained HFR values. Fixing the value of the exponent, we obtain the values of the severity factor function parameters which are listed in Table II with the factor in the Arrhenius-like exponential being $\alpha_{R_0} = 7994$ K. The functional form of the severity factor function, and the corresponding number of parameters, was incrementally modified until a satisfactory fit to the data could be obtained. The calibrated severity factor function model (12) is plotted in Fig. 14. The HFR

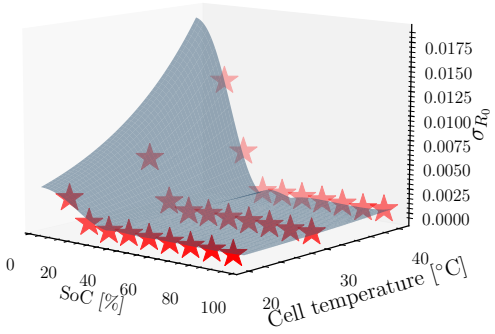

Fig. 14: ***Cell resistance increase severity factor****. Calibrated severity factor function (blue surface) plotted as a function of SoC and cell temperature against obtained severity factor function values (stars). The parameter values used in (12) to generate the surface are listed in Table II.*

increase model predictions (11) are shown in Fig. 15 against the obtained HFR values. The models successfully captures the inferred observed resistance increase for most SoCs $> 25\%$.

TABLE II: Parameter values that define the HFR increase severity factor function (12).

i	0	1	2	3	4
θ_{1i}	1.56	-6.14	1.76	6.93	3.53
θ_{2i}	25.51	3.67	-4.57	-32.72	28.85

APPENDIX B
CELL VALIDATION RESULTS

Here we validate the battery cell model by comparing its outputs to experimental data at three different ambient temperature conditions and reference performance tests (RPTs), i.e. at different stages of aging. The experimental data consists of a dynamic stress test profile input (Fig. 16) designed to discharge 60% of the cell's energy and the outputs are the cell voltage and surface temperature. Figure 17 shows this comparison for the cell voltage while Fig. 18 shows it for the cell temperature. The battery cell model obtains good agreement with the experimental data with sub-1% error in both the voltage and the temperature.

APPENDIX C
BATTERY PACK THERMAL MODEL CALIBRATION

In this section, we detail how the thermal model, governing the heat exchange between cells and modules as explained

This article has been accepted for publication in IEEE Transactions on Transportation Electrification. This is the author's version which has not been fully edited and content may change prior to final publication. Citation information: DOI 10.1109/TTE.2024.3365028

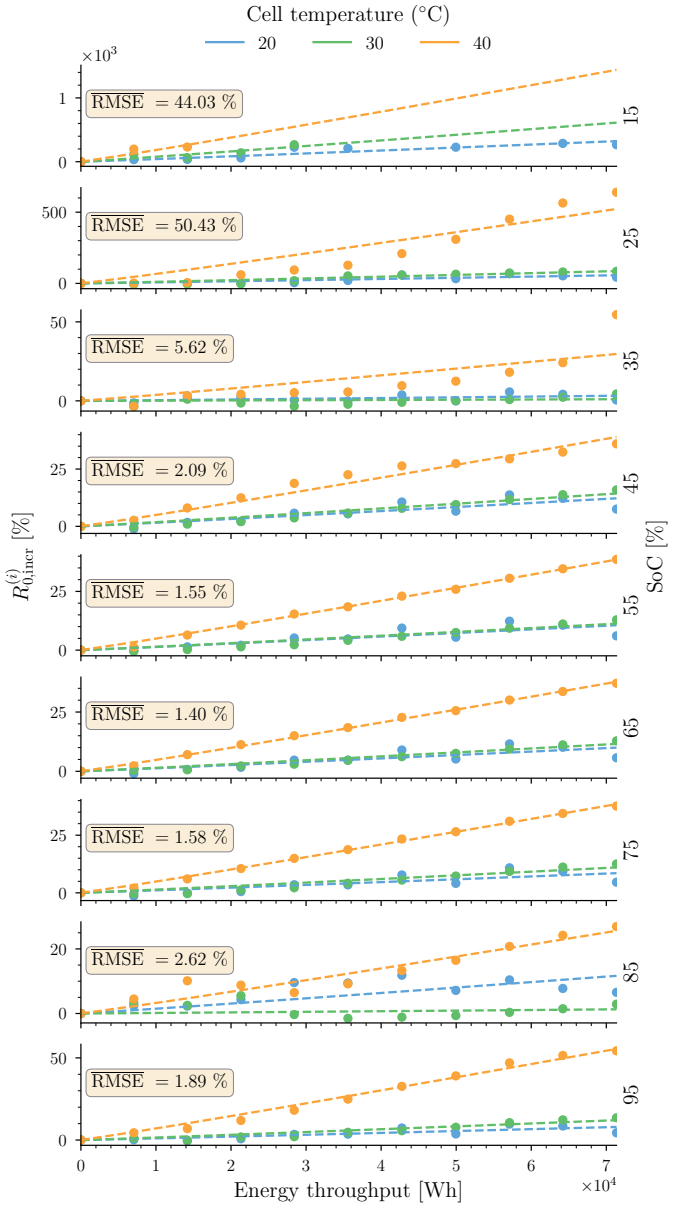

Fig. 15: ***The normalized high-frequency resistance increase cell aging data is described well by the proposed model*** *(11). The experimentally measured normalized HFR increase, shown in points, are obtained by the procedure described in the text. The aging model (11), with (12), is evaluated for the stated conditions and shown in lines. SoC value increases down the rows. Different colors denote different temperatures.*

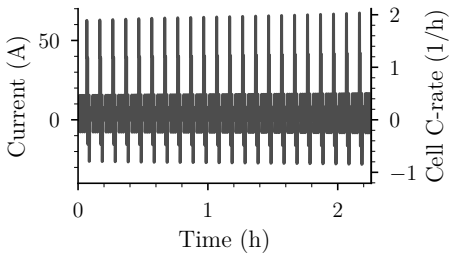

Fig. 16: The dynamic stress test current profile used for cell model validation [10].

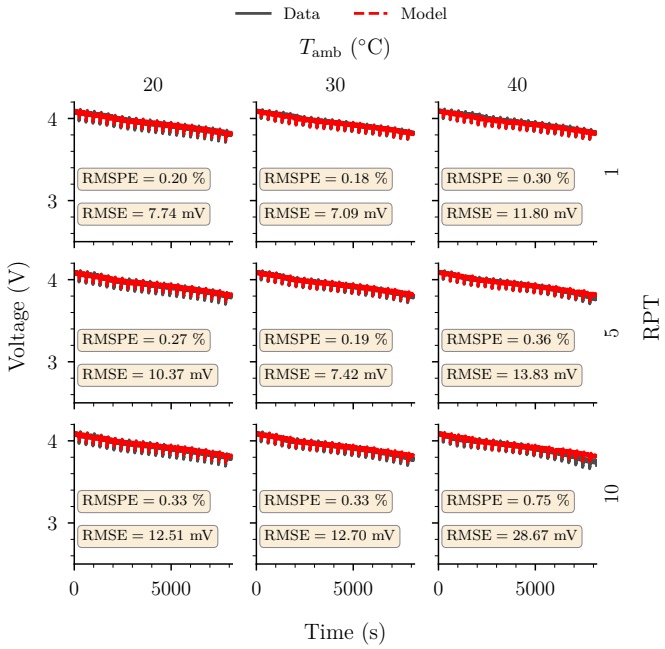

Fig. 17: ***Experimental voltage data corresponding to the dynamic stress test current (Fig. 16) is used to validate the electrical submodel of the battery cell model across a wide range of conditions.*** *Every subplot shows the experimental (solid dark curve) and the model (dashed red curve) voltage as a function of time. Variation of ambient conditions across columns. Variation of RPT number (correlated with the degree of aging) down the rows.*

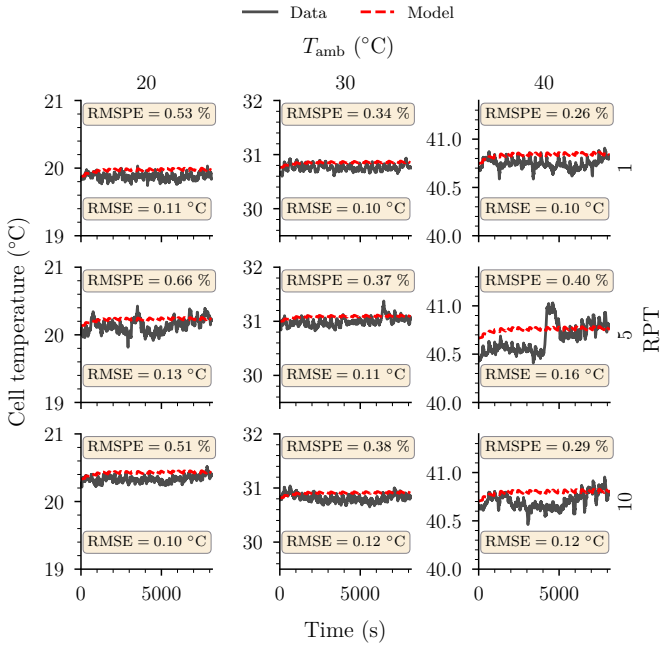

Fig. 18: ***Experimental temperature data corresponding to the dynamic stress test current (Fig. 16) is used to validate the thermal submodel of the battery cell model across a wide range of conditions.*** *Every subplot shows the experimental (solid dark curve) and the model (dashed red curve) temperature as a function of time. Same condition variation as in Fig. 17*

in Section IV-A is calibrated. We follow a similar procedure used to calibrate the battery cell submodels in Appendix A but use a different approach to optimization. Specifically, we minimize the RMSPE (25) between the model output for the average module temperature against the measured pack temperature from the first drive cycle data collected the beginning of the second month of the experiment. As the pack model is too computationally expensive for use in a population-based method like PSO, we instead perform a 3-stage parameter search. In the first stage, a grid search is performed allowing each of the battery pack thermal resistance parameters, R_{d}, R_{pm}, R_{mm}, R_{mc}, R_{mc}, to take the following values $\{10^{-1}, 10^{0}, 10^{1}\}$ holding the values of $C_{\mathrm{module}} = 10^{2}$ and $C_{\mathrm{pack}} = 10^{6}$. In the second stage, another grid search is performed allowing $C_{\mathrm{module}} \in \{10, 100, 500, 1000\}$ and $C_{\mathrm{pack}} \in \{10^{5}, 10^{6}, 10^{7}\}$ while holding the thermal resistances at the optimal values found from the first stage. Finally, in the third stage, an ad-hoc manual search is used and the parameters listed in Table III are found. The validation of the model is performed in Section IV-B using drive cycle data collected 10 days into the second month of the experiment.

TABLE III: Thermal model parameters.

Parameter	Value
C_{module} (kJ/°C)	0.4
C_{pack} (kJ/°C)	10,000
R_{cc} (°C/W)	0.25
R_{mm} (°C/W)	0.125
R_{pm} (°C/W)	1.0
R_{d} (°C/W)	0.5

REFERENCES

[1] Y. Ding, Z. P. Cano, A. Yu, J. Lu, and Z. Chen, "Automotive Li-Ion Batteries: Current Status and Future Perspectives," *Electrochem. Energ. Rev.*, vol. 2, pp. 1–28, Mar. 2019.

[2] W. Chen, J. Liang, Z. Yang, and G. Li, "A Review of Lithium-Ion Battery for Electric Vehicle Applications and Beyond," *Energy Procedia*, vol. 158, pp. 4363–4368, Feb. 2019.

[3] B. Spiller, N. Loshawala, and E. DeAngeli, "Medium- and Heavy-Duty Vehicle Electrification: Challenges, Policy Solutions, and Open Research Questions," tech. rep., Resources for the Future, Washington, DC, 2023.

[4] "Advanced Clean Fleets Regulation - Drayage Truck Requirements." https://ww2.arb.ca.gov/resources/fact-sheets/advanced-clean-fleets-regulation-drayage-truck-requirements, 2023.

[5] A. Kotz, K. Kelly, J. Lustbader, and B. Oakleaf, "Port of New York and New Jersey Drayage Electrifcation Analysis," tech. rep., National Renewable Energy Laboratory, Golden, CO, 2022.

[6] J. Garrido, E. Hidalgo, M. Barth, and K. Boriboonsomsin, "Home-Base Charging Load Profiles of Battery Electric Trucks Considering Tour Completion and Time-of-Use Rates," in *2023 IEEE ITEC*, (Detroit, MI, USA), pp. 1–5, IEEE, June 2023.

[7] "Annual Merit Review - Project L096-1568 - Analysis - Vivek Sujan." https://www.energy.gov/eere/vehicles/2023-vehicle-technologies-office-amr-presentations-program, 2023.

[8] H. Wang, S. Wang, X. Feng, X. Zhang, K. Dai, J. Sheng, Z. Zhao, Z. Du, Z. Zhang, K. Shen, C. Xu, Q. Wang, X. Sun, Y. Li, J. Ling, J. Feng, H. Wang, and M. Ouyang, "An experimental study on the thermal characteristics of the cell-to-pack system," *Energy*, vol. 227, p. 120338, 2021.

[9] R. Xiong, Q. Yu, W. Shen, C. Lin, and F. Sun, "A Sensor Fault Diagnosis Method for a Lithium-Ion Battery Pack in Electric Vehicles," *IEEE Trans. Power Electron.*, vol. 34, pp. 9709–9718, Oct. 2019.

[10] T. R. Tanim, M. G. Shirk, R. L. Bewley, E. J. Dufek, and B. Y. Liaw, "Fast charge implications: Pack and cell analysis and comparison," *J. Power Sources*, vol. 381, pp. 56–65, Mar. 2018.

[11] M. J. Brand, M. H. Hofmann, M. Steinhardt, S. F. Schuster, and A. Jossen, "Current distribution within parallel-connected battery cells," *J. Power Sources*, vol. 334, pp. 202–212, Dec. 2016.

[12] M. Dubarry, A. Devie, and B. Y. Liaw, "Cell-balancing currents in parallel strings of a battery system," *J. Power Sources*, vol. 321, pp. 36–46, July 2016.

[13] S.-L. Jeng, C. M. Tan, and P.-C. Chen, "Statistical distribution of Lithium-ion batteries useful life and its application for battery pack reliability," *J. Energy Storage*, vol. 51, p. 104399, July 2022.

[14] M. Ali, C. Da Silva, and C. Amon, "Multiscale Modelling Methodologies of Lithium-Ion Battery Aging: A Review of Most Recent Developments," *Batteries*, vol. 9, p. 434, Aug. 2023.

[15] A. Allam and S. Onori, "Characterization of aging propagation in Lithium-ion cells based on an electrochemical model," in *2016 ACC*, (Boston, MA, USA), pp. 3113–3118, IEEE, July 2016.

[16] G. Plett, *Battery Management Systems, Volume I: Battery Modeling*. Artech House Power Engineering Series, Artech House, 2015.

[17] R. Ahmed, J. Gazzarri, S. Onori, S. Habibi, R. Jackey, K. Rzemien, J. Tjong, and J. LeSage, "Model-Based Parameter Identification of Healthy and Aged Li-ion Batteries for Electric Vehicle Applications," *SAE Int. J. Alt. Power.*, vol. 4, pp. 233–247, Apr. 2015.

[18] X. Lin, H. E. Perez, S. Mohan, J. B. Siegel, A. G. Stefanopoulou, Y. Ding, and M. P. Castanier, "A lumped-parameter electro-thermal model for cylindrical batteries," *J. Power Sources*, vol. 257, pp. 1–11, July 2014.

[19] M. Petit, E. Prada, and V. Sauvant-Moynot, "Development of an empirical aging model for Li-ion batteries and application to assess the impact of Vehicle-to-Grid strategies on battery lifetime," *Appl. Energy*, vol. 172, pp. 398–407, June 2016.

[20] G. Suri and S. Onori, "A control-oriented cycle-life model for hybrid electric vehicle lithium-ion batteries," *Energy*, vol. 96, pp. 644–653, Feb. 2016.

[21] J. Park, W. A. Appiah, S. Byun, D. Jin, M.-H. Ryou, and Y. M. Lee, "Semi-empirical long-term cycle life model coupled with an electrolyte depletion function for large-format graphite/LiFePO 4 lithium-ion batteries," *J. Power Sources*, vol. 365, pp. 257–265, Oct. 2017.

[22] A. Chu, A. Allam, A. Cordoba Arenas, G. Rizzoni, and S. Onori, "Stochastic capacity loss and remaining useful life models for lithium-ion batteries in plug-in hybrid electric vehicles," *J. Power Sources*, vol. 478, p. 228991, Dec. 2020.

[23] K. Liu, X. Hu, Z. Wei, Y. Li, and Y. Jiang, "Modified Gaussian Process Regression Models for Cyclic Capacity Prediction of Lithium-Ion Batteries," *IEEE Trans. Transp. Electrific.*, vol. 5, pp. 1225–1236, Dec. 2019.

[24] K. A. Severson, P. M. Attia, N. Jin, N. Perkins, B. Jiang, Z. Yang, M. H. Chen, M. Aykol, P. K. Herring, D. Fraggedakis, M. Z. Bazant, S. J. Harris, W. C. Chueh, and R. D. Braatz, "Data-driven prediction of battery cycle life before capacity degradation," *Nat Energy*, vol. 4, pp. 383–391, May 2019.

[25] F. Dettù, G. Pozzato, D. M. Rizzo, and S. Onori, "Exergy-based modeling framework for hybrid and electric ground vehicles," *Applied Energy*, vol. 300, p. 117320, Oct. 2021.

[26] M. Jafari, A. Gauchia, K. Zhang, and L. Gauchia, "Simulation and Analysis of the Effect of Real-World Driving Styles in an EV Battery Performance and Aging," *IEEE Trans. Transp. Electrific.*, vol. 1, pp. 391–401, Dec. 2015.

[27] I. Mareev, J. Becker, and D. Sauer, "Battery Dimensioning and Life Cycle Costs Analysis for a Heavy-Duty Truck Considering the Requirements of Long-Haul Transportation," *Energies*, vol. 11, p. 55, Dec. 2017.

[28] G. Saldaña, J. I. San Martín, I. Zamora, F. J. Asensio, and O. Oñederra, "Analysis of the Current Electric Battery Models for Electric Vehicle Simulation," *Energies*, vol. 12, p. 2750, July 2019.

[29] A. Cordoba-Arenas, S. Onori, and G. Rizzoni, "A control-oriented lithium-ion battery pack model for plug-in hybrid electric vehicle cycle-life studies and system design with consideration of health management," *J. Power Sources*, vol. 279, pp. 791–808, Apr. 2015.

[30] C. Escobar, Z. Gong, C. Da Silva, O. Trescases, and C. H. Amon, "Effect of Cell-to-Cell Thermal Imbalance and Cooling Strategy on Electric Vehicle Battery Performance and Longevity," in *2022 21st IEEE iTherm Conf.*, (San Diego, CA, USA), pp. 1–9, IEEE, May 2022.

[31] I. Zilberman, J. Schmitt, S. Ludwig, M. Naumann, and A. Jossen, "Simulation of voltage imbalance in large lithium-ion battery packs influenced by cell-to-cell variations and balancing systems," *J. Energy Storage*, vol. 32, p. 101828, Dec. 2020.

[32] A. Fill, S. Koch, and K. P. Birke, "Analytical model of the current distribution of parallel-connected battery cells and strings," *J. Energy Storage*, vol. 23, pp. 37–43, June 2019.
[33] A. Allam, S. Onori, S. Marelli, and C. Taborelli, "Battery Health Management System for Automotive Applications: A retroactivity-based aging propagation study," in *2015 ACC*, (Chicago, IL, USA), pp. 703–716, IEEE, July 2015.
[34] "Nissan LEAF Teardown: Lithium-ion battery pack structure." https://www.marklines.com/en/report/rep1786_201811, 2018.
[35] M. Shirk and J. Wishart, "Effects of Electric Vehicle Fast Charging on Battery Life and Vehicle Performance," in *SAE 2015 World Congress & Exhibition*, pp. 2015–01–1190, Apr. 2015.
[36] G. Plett, *Battery Management Systems, Volume II: Equivalent-Circuit Methods*. Artech House power engineering and power electronics, Artech House, 2015.
[37] C. Forgez, D. Vinh Do, G. Friedrich, M. Morcrette, and C. Delacourt, "Thermal modeling of a cylindrical LiFePO4/graphite lithium-ion battery," *J. Power Sources*, vol. 195, pp. 2961–2968, May 2010.
[38] J. Li and M. S. Mazzola, "Accurate battery pack modeling for automotive applications," *J. Power Sources*, vol. 237, pp. 215–228, Sept. 2013.
[39] S. Ha, G. Pozzato, and S. Onori, "Electrochemical characterization tools for lithium-ion batteries," *J. Solid State Electrochem.*, Nov. 2023.
[40] L. Serrao, S. Onori, G. Rizzoni, and Y. Guezennec, "A Novel Model-Based Algorithm for Battery Prognosis," *IFAC Proceedings Volumes*, vol. 42, no. 8, pp. 923–928, 2009.
[41] T. Bergman, A. Lavine, F. Incropera, and D. DeWitt, *Fundamentals of Heat and Mass Transfer*. Wiley, 2020.
[42] K. Rumpf, M. Naumann, and A. Jossen, "Experimental investigation of parametric cell-to-cell variation and correlation based on 1100 commercial lithium-ion cells," *J. Energy Storage*, vol. 14, pp. 224–243, Dec. 2017.
[43] Z. Song, X.-G. Yang, N. Yang, F. P. Delgado, H. Hofmann, and J. Sun, "A study of cell-to-cell variation of capacity in parallel-connected lithium-ion battery cells," *eTransportation*, vol. 7, p. 100091, Feb. 2021.
[44] "BU-908: Battery Management Systems (BMS)." https://batteryuniversity.com/article/bu-908-battery-management-system-bms, 2019.
[45] Z. Wang, Z. Wang, J. Davidson, M. Foster, and D. Gladwin, "A Monte Carlo simulator to investigate cell-to-cell deviation in a grid-tied battery pack," *IET Power Electron.*, vol. 15, pp. 1264–1278, Oct. 2022.
[46] M. Kochenderfer and T. Wheeler, *Algorithms for Optimization*. MIT Press, 2019.

Joseph N. E. Lucero (Student Member, IEEE) is currently a Ph.D. candidate in the Department of Chemistry at Stanford University where his research focuses on modeling of Li-ion batteries and developing electrochemical-based estimation algorithms for next-generation battery management systems. He received his Bachelor of Science degree (with Distinction) in Biological Physics in 2019 and his Master of Science degree in Physics in 2021, both from Simon Fraser University in British Columbia, Canada.

Vivek A. Sujan (Senior Member, IEEE) has over 20 years of experience in developing and commercializing advanced powertrain, vehicle systems, and system-of-system technologies focused on automation, safety, reducing emissions and decarbonization of commercial vehicles. His work is focused on Hydrogen and Electrification Power Systems for On-/Off-Highway and intermodal applications. He is currently advancing decarbonization research of commercial vehicles and supporting ecosystems at the National Transportation Research Center (NTRC), Oak Ridge National Laboratory. Prior to this, he had been with Cummins Inc. for nearly 18 years, where he was the Senior Technical Director leading broad cross-functional teams on Advanced Technology Planning and Development for the New Power Business Unit (NPBU, Cummins). At Cummins, he has also held several positions within the Engine Business Unit and Research & Technology Department. Prior to working at Cummins, Dr. Sujan worked as a Post-Doctoral Research Engineer at MIT/JPL-NASA for about 2 years, developing control architectures for robotic systems in terrestrial and extra-terrestrial activities. Dr. Sujan received his B.S. degrees in Physics, Mathematics (1995) and Mechanical Engineering (1996) from CalTech, M.S. degree in Mechanical Engineering (1998), and a Ph.D. in Mechanical Engineering/Control Systems (2002) from MIT. He has over 70 internationally published papers and over 240 patents granted in the fields of Vehicles and Eco-Systems, Diesel engines, System Dynamics, Powertrains, Automation, and Controls.

Simona Onori (Senior Member, IEEE) is an Associate Professor of Energy Science and Engineering at Stanford University. She is a Fellow of SAE. She is the recipient of various awards, including the 2021 IEEE Transactions on Control Systems Technology (TCST) Outstanding Paper Award (as advisor), 2020 U.S. DOE C3E Award in the research category, 2017 NSF CAREER Award. She has been serving as the Editor-in-Chief of the SAE International Journal of Electrified Vehicles since 2020 and Associate Editor of IEEE TCST since 2023. Dr. Onori received her Ph.D. degree in control engineering from the University of Rome "Tor Vergata".